

# High-Pressure Phase Diagram and Superionicity of Alkaline Earth Metal Difluorides

Claudio Cazorla\*<sup>1</sup> and Arun K. Sagotra

School of Materials Science and Engineering, UNSW Sydney, Sydney, NSW 2052, Australia

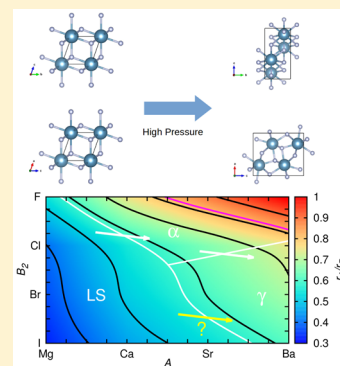
Meredith King

School of Materials Science and Engineering, North Carolina State University, Raleigh, North Carolina 27695, United States

Daniel Errandonea<sup>2</sup>

Departamento de Física Aplicada (ICMUV), Universitat de Valencia, 46100 Burjassot, Spain

**ABSTRACT:** We study the high-pressure–high-temperature phase diagram and superionicity of alkaline earth metal (AEM) difluorides ( $AF_2$ ,  $A = Ca, Sr, Ba$ ) with first-principles simulation methods. We find that the superionic behavior of  $SrF_2$  and  $BaF_2$  at high pressures differ appreciably from that previously reported for  $CaF_2$  [*Phys. Rev. Lett.* **2014**, *113*, 235902]. Specifically, the critical superionic temperature of  $SrF_2$  and  $BaF_2$  in the low-pressure cubic fluorite phase is not reduced by effect of compression, and the corresponding high-pressure orthorhombic contunnite phases become superionic at elevated temperatures. We get valuable microscopic insights into the superionic features of AEM difluorides in both the cubic fluorite and orthorhombic contunnite phases by means of *ab initio* molecular dynamics simulations. We rationalize our findings on the structural and superionic behavior of  $AF_2$  compounds in terms of simple ionic radii arguments and generalize them across the whole series of AEM dihalides ( $AB_2$ ,  $A = Mg, Ca, Sr, Ba$  and  $B = F, Cl, Br, I$ ) under pressure.



## I. INTRODUCTION

Fast-ion conductors (FIC) are materials that exhibit high ionic conductivity in the solid phase.<sup>1</sup> Examples of archetypal FIC, also known as superionic conductors, include alkali-earth metal fluorides ( $CaF_2$ ), oxides (doped  $CeO_2$ ), and lithium-rich compounds ( $Li_{10}GeP_2S_{12}$ ).<sup>1–3</sup> Inherent to superionicity is a significant increase in the concentration of point defects (e.g., Frenkel pair defects) associated with a particular sublattice of atoms in the crystal. Due to their unique ion-transport properties, FIC are promising materials for the realization of all-solid-state electrochemical batteries via replacement of customary liquid electrolytes, which involves substantial improvements with respect to standard batteries in terms of safety, cyclability, and electrochemical performance.<sup>4,5</sup> Owing to the large entropy change (typically of the order of  $100 \text{ J K}^{-1}$ ) and external tunability associated with the superionic phase transition,<sup>6</sup> FIC also are being established as auspicious calorific materials for exploitation in solid-state cooling applications.<sup>7–10</sup>

Recently, some of us studied the  $P$ – $T$  phase diagram of  $CaF_2$  (see Figure 1) and showed that this archetypal FIC presents some anomalous superionic behavior at high pressures.<sup>11</sup> At ambient conditions,  $CaF_2$  crystallizes in the cubic fluorite phase ( $\alpha$ , space group  $Fm\bar{3}m$ ) in which the  $Ca^{2+}$  ions are cubic coordinated to  $F^-$  ions (see Figure 2a). A sudden and large increase in the mobility of the fluorine ions is observed in  $\alpha$ - $CaF_2$  at  $T_s \approx 1400 \text{ K}$ ,<sup>12–16</sup> which is about 300 K below

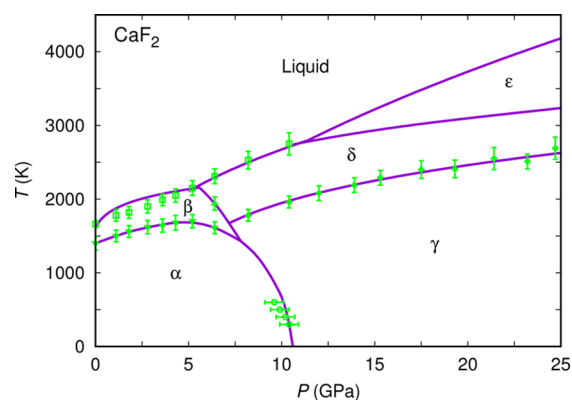


**Figure 1.** High- $P$ –high- $T$  phase diagram of  $CaF_2$  obtained with first-principles methods (adapted from ref 11). Dots and error bars correspond to experimental measurements also from ref 11. Letters  $\alpha$ ,  $\beta$ ,  $\gamma$ ,  $\delta$ , and  $\epsilon$  represent different phases (see text).

the corresponding melting temperature. Upon a compression of  $\sim 10 \text{ GPa}$  and at low temperatures,  $\alpha$ - $CaF_2$  transforms into an orthorhombic cotunnite phase ( $\gamma$ , space group  $Pnma$ ,

**Received:** November 7, 2017

**Revised:** December 11, 2017

**Published:** December 19, 2017

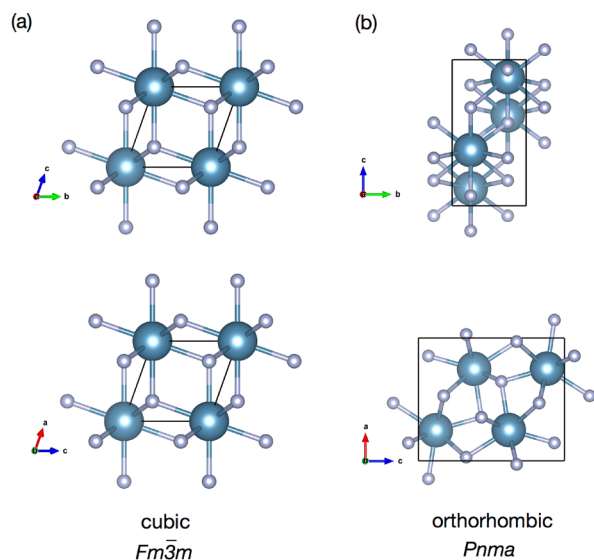


**Figure 2.** Sketch of the low- $T$  phases of alkali-earth metal difluorides observed at low and high pressures (cubic and orthorhombic, respectively).

see Figure 2b). Our previous experiments and first-principles simulations disclosed an unusual  $P$ -induced superionic effect in  $\alpha$ - $\text{CaF}_2$  that consists in a moderate lowering of  $T_s$  within the interval  $5 \leq P \leq 8$  GPa (see Figure 1). We also found that superionicity is absent in  $\gamma$ - $\text{CaF}_2$  but reappears in a low-symmetry high- $T$  phase, labeled as  $\delta$  in Figure 1, which is stabilized over  $\gamma$  via a  $T$ -induced second-order phase transition.<sup>11</sup> We tentatively indexed that  $\delta$  phase, which at high enough temperatures becomes superionic (phase  $\epsilon$  in Figure 1), as monoclinic (space group  $P2_1/c$ , see Figure 3a).

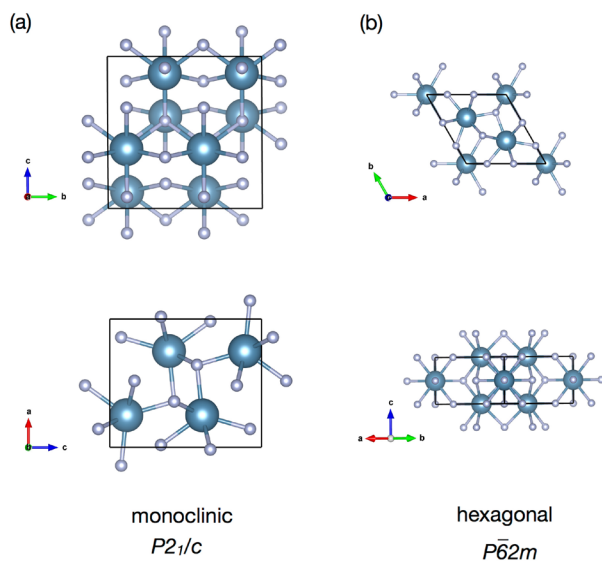


**Figure 3.** Sketch of the two candidate structures proposed for the  $\delta$  phase appearing in the phase diagram of  $\text{CaF}_2$  at high- $P$ –high- $T$  conditions. The monoclinic  $P2_1/c$  phase has been proposed by Cazorla and Errandonea<sup>11</sup> and the hexagonal  $P\bar{6}2m$  phase by Nelson et al.<sup>17</sup>

It is of great technological and fundamental interests to ascertain whether similar anomalous  $P$ -induced superionic phenomena than reported for  $\text{CaF}_2$  can occur also in other compounds of the alkaline earth metal (AEM) dihalides series,

$\text{AB}_2$  ( $A = \text{Mg, Ca, Sr, Ba}$  and  $B = \text{F, Cl, Br, I}$ ). For instance, as we have shown in other works,<sup>6–10</sup> the superionic trends induced by mechanical stress on conventional FIC may motivate new developments in the field of energy materials. Also, some AEM dihalides occur naturally as minerals (e.g.,  $\text{MgF}_2$  known as sellaite); hence, their high-pressure behavior is of interest in geophysics. Further, it remains to be determined what is the exact nature of the nonsuperionic  $\delta$  phase in  $\text{CaF}_2$ , and whether this phase appears or not in the high- $P$  phase diagram of other similar ionic compounds. Actually, in a recent paper by Nelson et al. it has been proposed, based on the outcomes of first-principles random structure searching and quasi-harmonic calculations, that the crystalline symmetry of the  $\delta$  phase could be hexagonal (space group  $P\bar{6}2m$ , see Figure 3b).<sup>17</sup>

In this work, we present a comprehensive first-principles study on the high- $P$ –high- $T$  phase diagrams and superionic properties of  $\text{SrF}_2$  and  $\text{BaF}_2$ . We also analyze the ionic-transport properties of  $\text{CaF}_2$  in the hexagonal  $P\bar{6}2m$  structure recently proposed by Nelson et al. for the  $\delta$  phase. Our *ab initio* molecular dynamics (AIMD) simulations based on density functional theory, which fully take into account anharmonicity, show that (i) the superionic transition temperatures of  $\alpha$ - $\text{SrF}_2$  and  $\alpha$ - $\text{BaF}_2$  never get depleted by effect of pressure, (ii) the  $\delta$  phase does not appear in the high- $P$ –high- $T$  phase diagrams of  $\text{SrF}_2$  and  $\text{BaF}_2$ , and (iii)  $\text{CaF}_2$  in the hexagonal  $P\bar{6}2m$  phase becomes vibrationally unstable at high temperatures and does not sustain superionicity (which is inconsistent with the phase diagram proposed in ref 11, see Figure 1). We discuss several fast-ion conduction mechanisms occurring in AEM difluorides at low and high pressures, based on the spatial arrangements of fluorine ions obtained in our AIMD simulations of the superionic phases  $\beta$  and  $\epsilon$ . Finally, in view of our results obtained for AEM difluorides and of additional first-principles calculations, we propose a generalized phase diagram for AEM dihalides ( $\text{AB}_2$ ,  $A = \text{Mg, Ca, Sr, Ba}$  and  $B = \text{F, Cl, Br, I}$ ) under pressure expressed as a function of a simple and physically intuitive parameter, the ionic radii ratio  $r_A/r_B$ .

This article is organized as follows. In the next section, we explain the details of our first-principles calculations and the strategy followed in the derivation of the high- $P$ –high- $T$  phase diagrams of  $\text{SrF}_2$  and  $\text{BaF}_2$ . Then, we report our results in section III and present a discussion on the structural trends of AEM dihalides under pressure in section IV. Finally, we summarize our main findings in section V.

## II. COMPUTATIONAL METHODS

**II.A. Density Functional Theory.** Our first-principles density functional theory (DFT) calculations were performed with the PBE generalized gradient approximation to the exchange-correlation energy<sup>18</sup> as is implemented in the VASP code.<sup>19</sup> We used the PAW method<sup>20</sup> to represent the ionic cores and considered AEM's 6p-2s, and F's 2s-5p electronic states as valence. Wave functions were represented in a plane-wave basis truncated at 650 eV. By using these parameters and dense  $k$ -point grids for integrations within the first Brillouin zone (i.e., of  $14 \times 14 \times 14$  for the  $\alpha$  and  $\gamma$  phases and of  $8 \times 8 \times 10$  for the hexagonal  $P\bar{6}2m$  phase), we obtained zero-temperature enthalpies converged to within 1 meV per formula unit. In the geometry relaxations, we imposed a force tolerance of  $0.01 \text{ eV}\cdot\text{\AA}^{-1}$ . Details of our vibrational phonon calculations and one-phase and coexistent *ab initio* molecular dynamics (AIMD) simulations are explained next.

**II.A.1. Vibrational Phonon Calculations.** Vibrational phonon frequencies were calculated with the direct approach.<sup>21,22</sup> In this method the force-constant matrix is directly calculated in real-space by considering the proportionality between the atomic displacements and forces when the former are sufficiently small. Large supercells then should be constructed in order to guarantee that the elements of the force-constant matrix have all fallen off to negligible values at their boundaries (a condition that follows from the use of periodic boundary conditions). Here, we employed simulation boxes of 192 atoms for the  $\alpha$  and  $\gamma$  phases and of 243 atoms for the hexagonal  $P\bar{6}2m$  phase. Dense  $\mathbf{k}$ -point grids were used for the calculation of the atomic forces with VASP (i.e., of  $4 \times 4 \times 4$  for the  $\alpha$  and  $\gamma$  phases and of  $3 \times 3 \times 4$  for the hexagonal  $P\bar{6}2m$  phase), and the computation of the corresponding pseudopotential nonlocal parts was performed in reciprocal space. We used the PHON code from Alfe<sup>23</sup> to obtain the vibrational phonon frequencies of the crystal phases at any arbitrary  $\mathbf{q}$  point and  $s$  branch,  $\omega_{\mathbf{q}s}$ . In doing this we exploited the translational invariance of the system to impose that the three acoustic branches are exactly zero at the  $\Gamma$  point, and used central differences in the atomic forces (that is, we considered both positive and negative atomic displacements). For a given phase, the corresponding Helmholtz free energy associated with the lattice vibrations,  $F^{\text{harm}}$ , then can be estimated within the quasi-harmonic approximation (QHA) by using the formula:<sup>24</sup>

$$F^{\text{harm}}(V, T) = \frac{1}{N_q} k_B T \sum_{\mathbf{q}s} \ln \left[ 2 \sinh \left( \frac{\hbar \omega_{\mathbf{q}s}(V)}{2k_B T} \right) \right] \quad (1)$$

where  $N_q$  is the total number of wave vectors used for integration in the Brillouin zone, and the dependence of the vibrational phonon frequencies on the volume is explicitly noted.

**II.A.2. Ab Initio Molecular Dynamics.** We performed *ab initio* molecular dynamics (AIMD) simulations of two types: one-phase (involving solid or superionic phases) and coexistence (involving liquid and superionic phases coexisting in thermodynamic equilibrium). One-phase simulations were performed in the canonical ( $N, V, T$ ) ensemble, while the coexistence simulations were done in the microcanonical ( $N, V, E$ ) ensemble. In the ( $N, V, T$ ) simulations, the temperature was kept fluctuating around a set-point value by using Nosé–Hoover thermostats. Large simulation boxes containing 192 (or 243) and 648 atoms were used in the one-phase and coexistence simulations, respectively. Periodic boundary conditions were applied along the three Cartesian directions in all the calculations. Newton's equations of motion were integrated by using the customary Verlet's algorithm and setting a time-step length of  $10^{-3}$  ps.  $\Gamma$ -point sampling for integration within the first Brillouin zone was employed in all our AIMD simulations.

Comprehensive one-phase ( $N, V, T$ ) molecular dynamics simulations were carried out in order to estimate the normal-superionic phase boundaries of AEM difluorides as a function of pressure. The calculations comprised long simulation times of up to  $\sim 30$  ps. We systematically ran the simulations at temperature intervals of 250 K by considering several volume points. Stabilization of the superionic state was ascribed to the thermodynamic conditions at which the diffusion coefficient of the fluorine ions,  $D$ , started to depart significantly from zero (see, for instance, refs 11 and 25 for some explicit examples).

Specifically, the diffusion coefficient of each ionic species was determined as

$$D = \lim_{t \rightarrow \infty} \frac{\langle |\mathbf{r}_i(t + t_0) - \mathbf{r}_i(t_0)|^2 \rangle}{6t} \quad (2)$$

where  $\mathbf{r}_i(t)$  is the position of the migrating ion labeled as  $i$  at time  $t$ ,  $t_0$  an arbitrary time origin, and  $\langle \dots \rangle$  denotes average over time origins  $t_0$  and particles of the same species. Meanwhile, the mean squared displacement (MSD) is equal to  $\langle \Delta \mathbf{r}_i^2(t) \rangle \equiv \langle |\mathbf{r}_i(t + t_0) - \mathbf{r}_i(t_0)|^2 \rangle$ . We should note that our superionic transition temperature results, in principle, could be affected by some *superheating* bias.<sup>26</sup> However, due to the second-order nature of the superionic phase transition in AEM difluorides,<sup>1</sup> those errors are likely to be very small in practice. In fact, we performed several molecular dynamics tests in  $\text{CaF}_2$  under pressure by using the rigid-ion empirical potential and techniques reported in ref 6 and concluded that the typical size of the accompanying normal–superionic hysteresis is well below 100 K (which corresponds to our numerical accuracy in the determination of superionic transition temperatures).

To ascertain that the crystal remained vibrationally stable (that is, the thermal average position of each ion remains centered on its perfect-lattice site), we computed the position correlation function defined as<sup>11,27</sup>

$$p(t) = \langle (\mathbf{r}_i(t + t_0) - \mathbf{R}_i^0) \cdot (\mathbf{r}_i(t_0) - \mathbf{R}_i^0) \rangle \quad (3)$$

where  $\mathbf{R}_i^0$  corresponds to the perfect-lattice position of the  $i^{\text{th}}$  atom and, again,  $\langle \dots \rangle$  denotes average over time origins  $t_0$  and ions of the same species. The crystal is vibrationally stable if  $p(t \rightarrow \infty) = 0$  since the displacements at widely separated times become uncorrelated. On the contrary, if the atoms acquire a permanent vibrational displacement,  $p(t \rightarrow \infty)$  becomes nonzero.

Following previous works,<sup>27–32</sup> we performed comprehensive ( $N, V, E$ ) coexistence simulations in order to determine the melting curve of AEM difluorides as a function of pressure.<sup>33</sup> A supercell containing the perfect crystal structure (that is, either the fluorite or contunnite phase) was first thermalized at a temperature slightly below the expected melting temperature for about 4 ps. The system remained in a superionic state. The simulation then was halted, and the positions of the atoms in one-half of the supercell were held fixed, while the other half was heated up to a very high temperature (typically five times the expected melting temperature) for about 4 ps, so that it melted completely. With the fixed atoms still fixed, the molten part was rethermalized to the expected melting temperature (for about 2 ps). Finally, the fixed atoms were released, thermal velocities were assigned, and the whole system was allowed to evolve freely at constant ( $N, V, E$ ) for a long time (normally more than 20 ps), so that the solid and liquid come into equilibrium (likewise, this final step can be performed in the ( $N, P, H$ ) ensemble so as to choose the hydrostatic pressure conditions<sup>34,35</sup>). The system was monitored by calculating the average number of particles in slices of the cell taken parallel to the initial solid–liquid interface. With this protocol, there is a certain amount of trial and error to find the overall volume that yields a two-phase coexisting system. Examples of successful coexistence runs can be found, for instance, in refs 11, 27, and 28.

**II.B. Derivation of the Phase Diagrams.** The high- $P$ –high- $T$  phase diagram of  $\text{CaF}_2$  shown in Figure 1 has been adapted from ref 11; full details on how this was derived can

be found in the corresponding reference. As regards SrF<sub>2</sub> and BaF<sub>2</sub>, the corresponding high-*P*–high-*T* phase diagrams reported in Figures 7 and 8 were obtained as follows.

First, the zero-temperature  $\alpha \rightarrow \gamma$  transition pressure,  $P_{\alpha \rightarrow \gamma}(0)$ , was determined through standard DFT enthalpy (*H*) calculations. Subsequently, we estimated the normal to superionic phase boundaries corresponding to the  $\alpha$  and  $\gamma$  phases over wide *P*–*T* intervals by using one-phase AIMD simulations (see section II.A.2). A total of 6  $\alpha$ – $\beta$  and 6  $\gamma$ – $\epsilon$  coexistence points were determined in each compound, to which spline curves were fitted. The melting lines of the two resulting superionic phases,  $\beta$  and  $\epsilon$ , were then determined by means of coexistence AIMD simulations (see section II.A.2). A total of three  $\beta$ –liquid and three  $\epsilon$ –liquid coexistence points were determined in each compound, to which spline curves were fitted. The point at which the  $\beta$ –liquid and  $\epsilon$ –liquid lines intersect corresponds to a three-fold coexistence state in which the Gibbs free-energy of the liquid,  $\beta$ , and  $\epsilon$  phases are equal. Such a thermodynamic state, therefore, belongs also to the coexistence line of the  $\beta$  and  $\epsilon$  phases. In order to draw the entire  $\beta$ – $\epsilon$  phase boundary, we made two simplifications, namely, (1) we assumed that the corresponding  $dT/dP$  slope was constant, and (2) rather than performing AIMD simulations, we fitted semiempirical potentials of the Born–Mayer–Huggins form (BMH, see Appendix) to relevant sets of DFT data and calculated with them the value of the  $\beta$ – $\epsilon$  phase boundary slope at the corresponding three-fold coexistence points; for this, we used classical molecular dynamics simulations and the Clausius–Clapeyron relation (see ref 25). By drawing the full  $\beta$ – $\epsilon$  coexistence line, we found the intersection point with the  $\gamma$ – $\epsilon$  phase boundary previously calculated with AIMD simulations. This provided us with a second (approximate) three-fold coexistence state involving the  $\beta$ ,  $\epsilon$ , and  $\gamma$  phases. In order to estimate the entire  $\beta$ – $\gamma$  coexistence line, we applied again the two approximations used in the derivation of the  $\beta$ – $\epsilon$  phase boundary. By drawing the full  $\beta$ – $\gamma$  phase boundary, we found a third (approximate) three-fold point involving coexistence of the  $\alpha$ ,  $\beta$ , and  $\gamma$  phases. Finally, we connected the latter three-fold coexistence state with the initial zero-temperature  $P_{\alpha \rightarrow \gamma}(0)$  point via a straight line (we note that this approximation is definitely unrealistic in the  $T \rightarrow 0$  limit as the value of the  $dT/dP$  slope diverges at such conditions).

### III. RESULTS

**III.A. Phase Diagrams.** Here, we discuss several aspects related to the identification of the  $\delta$  phase in CaF<sub>2</sub> (see Figure 1) and report the high-*T*–high-*P* phase diagrams of SrF<sub>2</sub> and BaF<sub>2</sub> as obtained with first-principles calculations (see Figures 7 and 8). Comparison to experiments are provided whenever measurements are available.

**III.A.1. Calcium Difluoride.** Nelson et al.<sup>17</sup> have recently proposed that the symmetry of  $\delta$ -CaF<sub>2</sub> could be hexagonal (space group  $P\bar{6}2m$ , see Figure 3b), based on the results of first-principles random structure searching and quasi-harmonic calculations. Previously, some of us tentatively indexed the same structure as monoclinic  $P2_1/c$  (Figure 3a).<sup>11</sup> Therefore, it seems interesting to further compare and analyze the superionic and thermodynamic stability properties of both candidate phases at high-*P*–high-*T* conditions.

Our zero-temperature enthalpy and quasi-harmonic Helmholtz free energy calculations are consistent with Nelson et al.'s results on the relative thermodynamic stability of the candidate hexagonal  $P\bar{6}2m$  phase as compared to the orthorhombic

(contunnite)  $Pnma$  phase. In particular, we estimate a small enthalpy energy difference of about 50 meV/f.u., favoring the contunnite phase, within the pressure interval  $15 \leq P \leq 55$  GPa at zero temperature. Also, the vibrational lattice properties of the hexagonal  $P\bar{6}2m$  phase (see Figure 4b) translate into

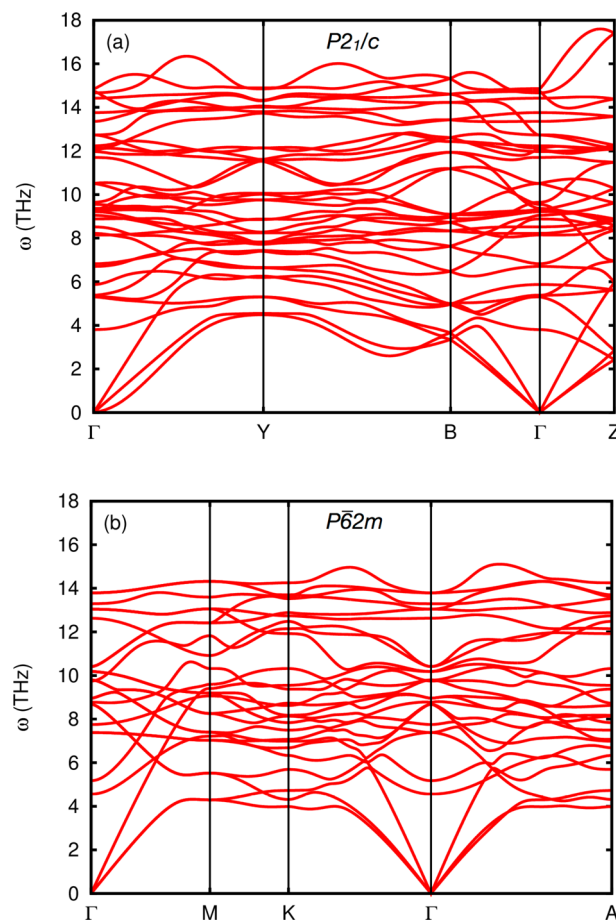


**Figure 4.** Vibrational phonon frequencies of CaF<sub>2</sub> calculated in different structures at  $P = 25$  GPa. (a) Monoclinic  $P2_1/c$  phase proposed by Cazorla and Errandonea.<sup>11</sup> (b) Hexagonal  $P\bar{6}2m$  phase proposed by Nelson et al.<sup>17</sup>

favorable Helmholtz free energies (eq 1) that could possibly render a *T*-induced stabilization over the orthorhombic  $Pnma$  phase at high pressures (see Figure 5). Meanwhile, our vibrational phonon calculations in the monoclinic  $P2_1/c$  phase clearly show that this structure is vibrationally stable (see Figure 4a) and different from the orthorhombic  $Pnma$  phase (see Figure 5). We must acknowledge, however, that the calculated quasi-harmonic (QHA) Helmholtz free energies turn out to favor the hexagonal  $P\bar{6}2m$  phase over the monoclinic  $P2_1/c$  (see Figure 5). The reason for this is that the medium- and high-frequency vibrational eigenmodes in the hexagonal  $P\bar{6}2m$  phase have smaller energies (see Figure 4). Therefore, in view of the results obtained with zero-temperature enthalpy and QHA Helmholtz free energy calculations, it seems reasonable to think that  $\delta$ -CaF<sub>2</sub> could possess hexagonal symmetry.

Nevertheless, as we already know from other materials,<sup>27,36–39</sup> the QHA approximation may fail at providing the right thermodynamic stability balance between different crystal structures at high-*P*–high-*T* conditions. Such a limitation may be specially critical in the present case since we are dealing with FIC that

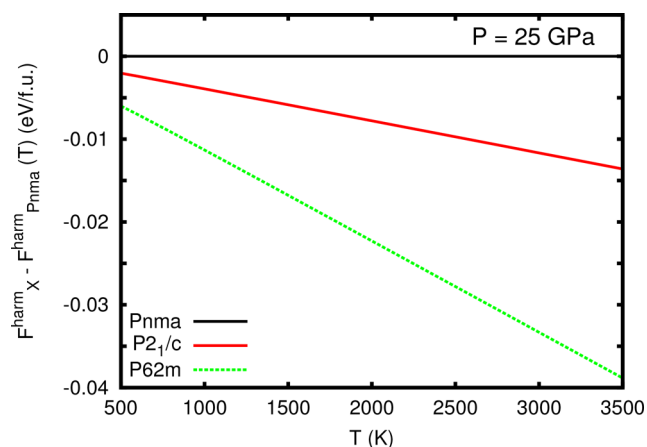


**Figure 5.** Quasi-harmonic Helmholtz free energy difference between several phases in  $\text{CaF}_2$  calculated at high- $P$  conditions and expressed as a function of temperature.

in the superionic state cannot be described with harmonic or quasiharmonic models. In order to analyze the vibrational stability and superionic properties of  $\text{CaF}_2$  in the hexagonal  $P\bar{6}2m$  phase while fully considering anharmonic effects, we performed extensive one-phase *ab initio* molecular dynamics (AIMD) simulations (see section II.A.2; in this case, we employed a simulation cell containing 243 atoms). Some of our AIMD results obtained at conditions  $P = 20(1)$  GPa and  $2000 \leq T \leq 3000$  K are shown in Figure 6. Several conclusions

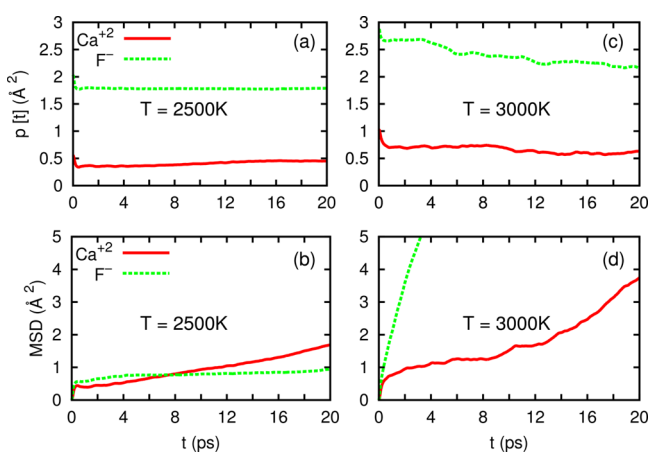


**Figure 6.** Position correlation function and mean squared displacement of  $\text{CaF}_2$  in the hexagonal  $P\bar{6}2m$  structure proposed by Nelson et al. for the  $\delta$  phase.<sup>17</sup> AIMD simulations were performed at  $P = 20(1)$  GPa and  $T = 2500$  K (a,b) and  $3000$  K (c,d).

can be drawn from the mean squared displacement and position correlation function,  $p(t)$ , plots (see section II.A.2) therein. First, at  $T = 2500$  K, the system becomes vibrationally unstable as the value of the  $p(t)$ 's calculated for the calcium and fluorine ions clearly depart from zero at large simulation times; actually, a certain diffusion of the  $\text{Ca}^{2+}$  ions is observed that cannot be identified with superionicity (namely, in the superionic state, the  $\text{F}^-$  ions are the mobile atoms instead). Upon a further increase in temperature, the system melts completely in our AIMD simulations (see Figure 6c,d). This outcome implies that due to likely *superheating* effects<sup>26</sup> the true melting point of  $\text{CaF}_2$  in the hexagonal  $P\bar{6}2m$  phase is lower than  $3000$  K,<sup>28</sup> which lays well below the melting point estimated for the

$\epsilon$  phase at equivalent pressure conditions, namely,  $T_m \approx 3500$  K (see Figure 1). These findings show that the hexagonal phase proposed by Nelson et al. does not reproduce the phase stability and superionic features of  $\text{CaF}_2$  at high- $P$ –high- $T$  conditions, as reported in ref 11.

It is worth noting in passing that Nelson et al. have also proposed a tentative normal–superionic phase boundary for the hypothesized  $\delta$  phase with hexagonal  $P\bar{6}2m$  symmetry. In particular, the authors determined first the zero-temperature threshold volume at which the hexagonal  $P\bar{6}2m$  phase starts to develop some vibrational lattice instabilities in the form of imaginary phonon eigenfrequencies,  $V_{\text{inst},j}$  subsequently, for a given pressure and by using QHA calculations, Nelson et al. found the temperature at which the volume of the system equals such a threshold volume, namely,  $V(P, T_c) = V_{\text{inst}}$ . The series of  $T_c$ 's obtained so by considering different pressure points were then ascribed to a tentative normal–superionic coexistence line. Several comments are in order. First, FIC are highly anharmonic systems; hence, as we have just demonstrated, QHA approaches appear to be highly inadequate for describing this class of materials at high temperatures. Second, Nelson et al.'s strategy for determining critical superionic points virtually would ascribe normal–superionic coexistence lines to most existing materials under pressure, as due to the ordinary occurrence of zero-temperature spinodal points and positive thermal expansions in crystals. However, as a matter of fact, only relatively few compounds involving specific ionic species and atomic arrangements exhibit fast-ion transport in practice.<sup>1–3</sup> (For instance, we note that according to our AIMD simulations  $\text{CaF}_2$  in the hexagonal  $P\bar{6}2m$  phase never becomes superionic.) Therefore, in general, we strongly discourage the use of QHA approaches for the prediction and screening of possible superionic compounds.

**III.A.2. Strontium Difluoride.** Figure 7 shows the high- $P$ –high- $T$  phase diagram of  $\text{SrF}_2$  as obtained with the first-principles

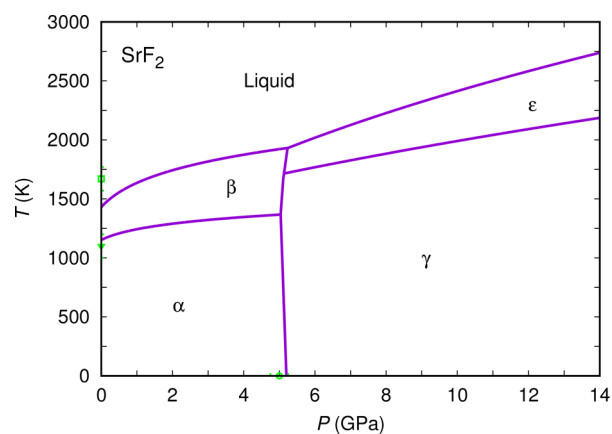


**Figure 7.** High- $P$ –high- $T$  phase diagram of  $\text{SrF}_2$  obtained with first-principles methods. Dots and error bars correspond to experimental measurements from refs 41 and 42. Letters  $\alpha$ ,  $\beta$ ,  $\gamma$ , and  $\epsilon$  represent different phases (see text).

methods and strategy described in section II. We find very good agreement with respect to the experiments for the  $\alpha \rightarrow \gamma$  transition pressure measured at low temperatures, and the  $\alpha \rightarrow \beta$  and  $\beta \rightarrow$  liquid transition temperatures measured at low pressures<sup>40–42</sup> (see Table 1). As compared to  $\text{CaF}_2$ , all three transition points hold smaller values, in special, that of the pressure-induced  $\alpha \rightarrow \gamma$  transformation occurring at low tem-

**Table 1. Comparison of the First-Principles Results Reported in the Present Study with the Experimental Data Found in Refs 40–42<sup>a</sup>**

$T_{m,0}$ (K)	$T_{m,0}^{\text{expt}}$ (K)	$T_{s,0}$ (K)	$T_{s,0}^{\text{expt}}$ (K)
		CaF <sub>2</sub>	
1660 (100)	1690 (100) <sup>40</sup> 1660 (100) <sup>11</sup>	1400 (100)	1370 (100) <sup>40</sup> 1400 (100) <sup>11</sup>
		SrF <sub>2</sub>	
1430 (100)	1740 (100) <sup>40</sup> 1670 (100) <sup>41</sup>	1150 (100)	1380 (100) <sup>40</sup> 1100 (100) <sup>42</sup>
		BaF <sub>2</sub>	
1350 (100)	1620 (100) <sup>40</sup> 1560 (100) <sup>41</sup>	1135 (100)	1245 (100) <sup>40</sup>

<sup>a</sup>CaF<sub>2</sub> results from ref 11 have been included for completeness.  $T_{m,0}$  and  $T_{s,0}$  stand for the melting and superionic transition temperatures obtained at  $P = 0$ , respectively. Figures within parentheses represent the precision in the calculations and experiments.

peratures. We predict up to three different multiphase coexistence points involving the trios  $\beta$ –liquid– $\epsilon$ ,  $\beta$ – $\gamma$ – $\epsilon$ , and  $\alpha$ – $\beta$ – $\gamma$  at (5.25 GPa, 1935 K), (5.10 GPa, 1710 K), and (5.00 GPa, 1365 K), respectively. The slopes of the  $\alpha$ – $\beta$  and  $\gamma$ – $\epsilon$  phase boundaries are small, positive, and practically constant as a function of pressure (that is, 43(2) and 53(2) K GPa<sup>-1</sup> in average, respectively). As regards melting, we estimate a  $dT_m/dP$  value of 330(10) K GPa<sup>-1</sup> at zero pressure (to be compared with 480(10) K GPa<sup>-1</sup> obtained in CaF<sub>2</sub> under equivalent conditions). Unfortunately, we have not found in the literature any measurements on the melting or fast-ion conduction properties of SrF<sub>2</sub> at high- $P$ –high- $T$  conditions to which compare our results.

Interestingly, we observe that the superionic behavior of highly compressed SrF<sub>2</sub> differs appreciably from that of CaF<sub>2</sub> as reported in ref 11 (see Figures 1 and 7). Specifically, in SrF<sub>2</sub> (1) the  $\alpha$ – $\beta$  coexistence line does not get depleted by the effect of pressure, and (2) the  $\delta$  phase does not appear in the corresponding phase diagram (that is, the  $\gamma$  phase, which is orthorhombic with space group  $Pnma$ , transforms directly into the superionic phase  $\epsilon$  at elevated temperatures). Previously, we correlated the anomalous superionic behavior observed in  $\alpha$ -CaF<sub>2</sub> with a  $P$ -induced softening of a zone-boundary phonon eigenmode involving displacements of fluorine ions only.<sup>11</sup> Such a vibrational phonon eigenmode softening is not observed in  $\alpha$ -SrF<sub>2</sub> under pressure; hence, our original hypothesis appears to be reinforced. Regarding the absence of the  $\delta$  phase in the phase diagram of SrF<sub>2</sub>, we tentatively rationalize this effect in terms of simple ionic radii arguments as follows.

AEM difluorides, AF<sub>2</sub>, naturally tend toward a superionic state at high temperatures, even when compressed. However, the contunnite  $\gamma$  phase presents a highly asymmetric ion-coordination environment that, as it has been suggested previously by other authors,<sup>43,44</sup> in principle does not allow for the creation of interstitial sites (or Frenkel defects), which are necessary for the triggering of fast-ion transport in type-II FIC.<sup>1,7–9</sup> That is the likely reason behind the stabilization of the  $\delta$  phase in CaF<sub>2</sub>, which can be described as a distorted version of the contunnite structure and where structural paths for ion migration open up in order to facilitate the stabilization of the superionic state ( $\epsilon$  phase) at high temperatures.<sup>11</sup> Nonetheless, if one considers  $A$  ions with larger ionic radii than Ca<sup>2+</sup> as compared to that of F<sup>-</sup>, namely,  $\eta(A) \equiv r_A/r_F > 0.75$ , then regions of excess volume appear within the contunnite structure (i.e., the packing

efficiency decreases) that may lower significantly the formation energy of point defects and accompanying energy barriers for ionic diffusion.<sup>6,8,9,45</sup> Consequently, the superionic state can be accessed directly from the contunnite  $\gamma$  phase at elevated temperatures. Such appears to be the case of SrF<sub>2</sub>, for which  $\eta(\text{Sr}) = 0.89$  and where the  $\delta$  phase is absent. Of our hypothesis to be correct, then the  $\delta$  phase should also be missing in the phase diagram of BaF<sub>2</sub> as  $\eta(\text{Ba}) > \eta(\text{Sr})$ . We will repeatedly comment on this point in the next sections.

**III.A.3. Barium Difluoride.** Figure 8 shows the high- $P$ –high- $T$  phase diagram of BaF<sub>2</sub> as obtained with the first-principles

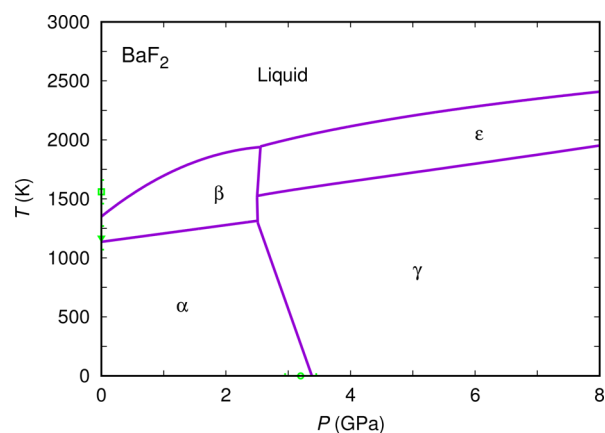


**Figure 8.** High- $P$ –high- $T$  phase diagram of BaF<sub>2</sub> obtained with first-principles methods. Dots and error bars correspond to experimental measurements from refs 40 and 41. Letters  $\alpha$ ,  $\beta$ ,  $\gamma$ , and  $\epsilon$  represent different phases (see text).

methods and strategy described in section II. We find good agreement with respect to the experiments for the  $\alpha \rightarrow \gamma$  transition pressure measured at low temperatures, and the  $\alpha \rightarrow \beta$  transition temperature measured at low pressures<sup>40,41</sup> (see Table 1); our estimation of the  $\beta \rightarrow$  liquid transition at  $P = 0$ , however, appears to underestimate the measured melting point by about 300 K<sup>40,41</sup> (see Table 1). As compared to SrF<sub>2</sub> and CaF<sub>2</sub>, all three transition points present smaller values, in particular that of the  $P$ -induced  $\alpha \rightarrow \gamma$  transformation occurring at low temperatures. The systematic phase transition trends rendered by our calculations across the AEM difluoride series, therefore, appear to justify the use of  $\eta$ -based arguments in order to describe them. As in SrF<sub>2</sub>, we predict three multiphase coexistence points involving the trios  $\beta$ –liquid– $\epsilon$ ,  $\beta$ – $\gamma$ – $\epsilon$ , and  $\alpha$ – $\beta$ – $\gamma$  at (2.55 GPa, 1940 K), (2.50 GPa, 1525 K), and (2.52 GPa, 1315 K), respectively. The slopes of the  $\alpha$ – $\beta$  and  $\gamma$ – $\epsilon$  phase boundaries are small, positive, and practically constant as a function of pressure (that is, 70(2) and 80(2) K GPa<sup>-1</sup> in average, respectively). As regards melting, we estimate a  $dT_m/dP$  value of 420(10) K GPa<sup>-1</sup> at zero pressure (to be compared with 480(10) and 330(10) K GPa<sup>-1</sup> obtained for CaF<sub>2</sub> and SrF<sub>2</sub> at equivalent conditions). Unfortunately, we have not found in the literature any measurements on the melting or fast-ion conduction properties of BaF<sub>2</sub> at high- $P$ –high- $T$  conditions to which compare these results.

We find that the superionic behavior of highly compressed BaF<sub>2</sub> is very similar to that of SrF<sub>2</sub> but quite different from that of CaF<sub>2</sub> as reported in ref 11 (see Figures 1, 7, and 8). We note that no vibrational phonon eigenmode softening is found in  $\alpha$ -BaF<sub>2</sub> under pressure, in accordance (contrast) to what we observe in  $\alpha$ -SrF<sub>2</sub> ( $\alpha$ -CaF<sub>2</sub>). Meanwhile, the fact that

the  $\delta$  phase is also missing in the high- $P$ –high- $T$  phase diagram of  $\text{BaF}_2$  appears to validate our  $\eta$ -based arguments introduced in the previous section. In particular,  $\eta(\text{Ba})$  amounts to 1.02, which is about 14% larger than  $\eta(\text{Ca})$ ; hence, the consequent formation of excess volume within  $\gamma$ - $\text{BaF}_2$  (as compared to the analogous phase in  $\text{CaF}_2$ ) and direct stabilization of the superionic  $\epsilon$  phase at elevated temperatures.

**III.B. Superionicity.** In this section, we analyze the ionic trajectories generated in long AIMD simulations (of up to 50 ps duration) of the superionic phases of AEM difluorides at low and high pressures. Specifically, we present fluorine density plots constructed as in-plane  $\text{F}^-$  position histograms. For doing this, the simulation cell was divided into a number of parallel slices along its out-of-plane  $c$  (or,  $a$ ) direction (see Figure 9),

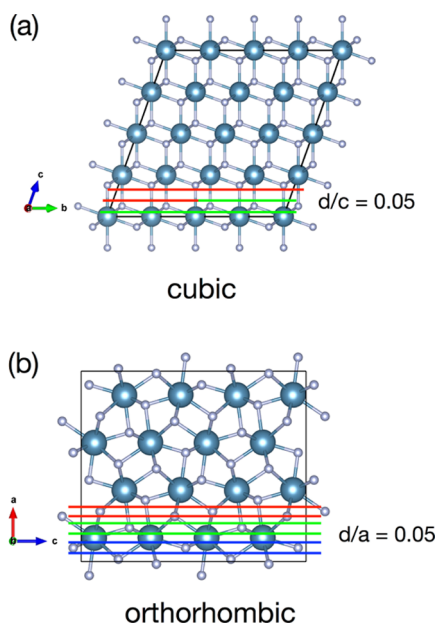


**Figure 9.** Sketch of the system (a, cubic; b, orthorhombic) partitions that have been set in order to construct the ionic density plots shown in the next three figures. Different colors indicate different system slices. The multicolor line in (a) stands for a same boundary belonging to two consecutive system partitions.

and the positions of the fluorine ions contained in them were projected over the  $a$ – $b$  (or  $b$ – $c$ ) plane. Averages were performed over time and ions. In order to facilitate the visualization of the preferred ionic diffusion paths, we considered fractional, rather than Cartesian, coordinates in our representations.

We also computed the incoherent scattering function of  $\text{F}^-$  ions,  $F_{\text{F}}(\mathbf{q}, t)$ , as in some cases that function can be measured directly in neutron scattering experiments. The intermediate scattering function is defined as the Fourier transform:<sup>46,47</sup>

$$F_{\alpha}(\mathbf{q}, t) = \int e^{i\mathbf{q}\cdot\mathbf{r}} G_{\alpha}(\mathbf{r}, t) \, d\mathbf{r} = \langle \exp[i\mathbf{q}\cdot\mathbf{r}_{\alpha}(t)] \rangle \quad (4)$$

where  $G_{\alpha}(\mathbf{r}, t) \, d\mathbf{r}$  is the probability that the displacement of an  $\alpha$ -ion will be found within a volume element  $d\mathbf{r}$  centered at  $\mathbf{r}$  at the time interval  $t$  [ $G_{\alpha}(\mathbf{r}, t)$  usually is known as the van Hove self-correlation function]. If the ionic species  $\alpha$  diffuses by discrete hops between sites, then at sufficiently long times  $F_{\alpha}(\mathbf{q}, t)$  behaves as a decaying exponential function,<sup>48</sup> namely:

$$\lim_{t \rightarrow \infty} F_{\alpha}(\mathbf{q}, t) \rightarrow \exp[-\gamma(\mathbf{q})t] \quad (5)$$

where  $\gamma(\mathbf{q})$  simply is a function of the wavevector  $\mathbf{q}$ .

**III.B.1. Cubic Fluorite Phase.** Figure 10 shows the fluorine density plots calculated in the low- $P$  superionic phase of  $\text{CaF}_2$

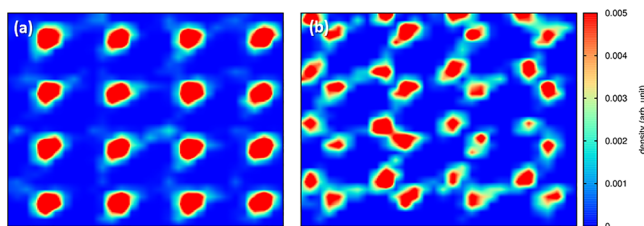


**Figure 10.** Fluorine density plots calculated with AIMD simulations in  $\text{CaF}_2$  in the superionic  $\beta$  phase at  $T = 1750$  K and  $P = 7.5$  GPa. Plots (a) and (b) were obtained by accumulating statistics over the two system partitions sketched in Figure 9a.

(equivalent results were obtained also in  $\beta$ - $\text{SrF}_2$  and  $\beta$ - $\text{BaF}_2$ , not shown here). The results presented in Figure 10a correspond to a system-slice containing one plane of fluorine equilibrium positions, as is shown by the simple-cubic arrangement rendered by the high-density areas therein. Meanwhile, the results presented in Figure 10b correspond to a system-slice situated between two consecutive  $\text{F}^-$  equilibrium position planes along the  $c$ -axis (see Figure 9a). The medium and high  $\text{F}^-$  density regions shown in Figure 10a,b, respectively, are both compatible with low-symmetry interstitial sites. In particular, the preferred non-equilibrium positions for fluorine ions correspond to  $(\frac{1}{2}, u, u)$  with  $u \approx 0.3$  and to  $(v, v, v)$  with  $v \approx 0.4$ , in pseudocubic notation, rather than to the more symmetric octahedral sites  $(\frac{1}{2}, \frac{1}{2}, \frac{1}{2})$ . These AIMD results are consistent with previous  $\text{CaF}_2$  molecular dynamics simulations performed with rigid-ion Born–Mayer–Huggins potentials<sup>6</sup> and neutron scattering measurements on fluorite-structured materials.<sup>49,50</sup>

The intermediate scattering function calculated in  $\beta$ - $\text{CaF}_2$  is shown in Figure 13a. (Function averages were performed over ions and time, by considering consecutive time origins within a 25 ps interval.) As can be observed therein,  $F_{\text{F}}$  decays as an exponential function at long simulation times (arbitrarily taken here as  $>10$  ps). This result indicates that superionicity in  $\beta$ - $\text{CaF}_2$  (and analogously in  $\beta$ - $\text{SrF}_2$  and  $\beta$ - $\text{BaF}_2$ , not shown here) in fact can be thought of as discrete and coordinated fluorine ion hops between neighboring interstitial sites. These AIMD results are also consistent with previous molecular dynamics simulations of fluorite-structured compounds performed with rigid-ion semi-empirical potentials.<sup>6,46</sup>

**III.B.2. Orthorhombic Contunnite Phase.** Figures 11 and 12 show the fluorine density plots calculated in the high- $P$  superionic phases of  $\text{CaF}_2$  and  $\text{SrF}_2$ , respectively (we note that equivalent results to those presented for  $\epsilon$ - $\text{SrF}_2$  were obtained also in  $\epsilon$ - $\text{BaF}_2$ , not shown here). The snapshots shown in those figures correspond to the  $\text{F}^-$  position histograms calculated in the three system slices represented in Figure 9b; as the contunnite phase has lower crystal symmetry than the fluorite phase, in this case several inequivalent  $\text{F}^-$  equilibrium positions appear projected within a same supercell partition. We note that the AIMD simulations from which those results were obtained were initialized from the perfect contunnite structure and lasted for about 50 ps. In  $\epsilon$ - $\text{SrF}_2$  (see Figure 12), the projected fluorine equilibrium positions render two triangular lattices shifted one with respect to the other (as given by the medium and high  $\text{F}^-$  density areas in the corresponding panels)

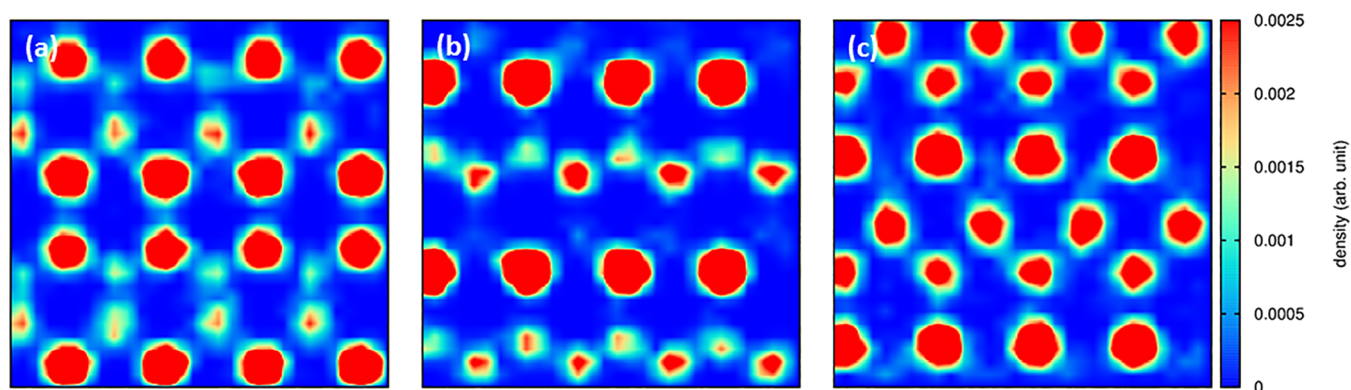


**Figure 11.** Fluorine density plots calculated with AIMD simulations in  $\text{CaF}_2$  in the superionic  $\epsilon$  phase at  $T = 3000$  K and  $P = 15$  GPa. Plots (a)–(c) were obtained by accumulating statistics over the three system partitions sketched in Figure 9b.

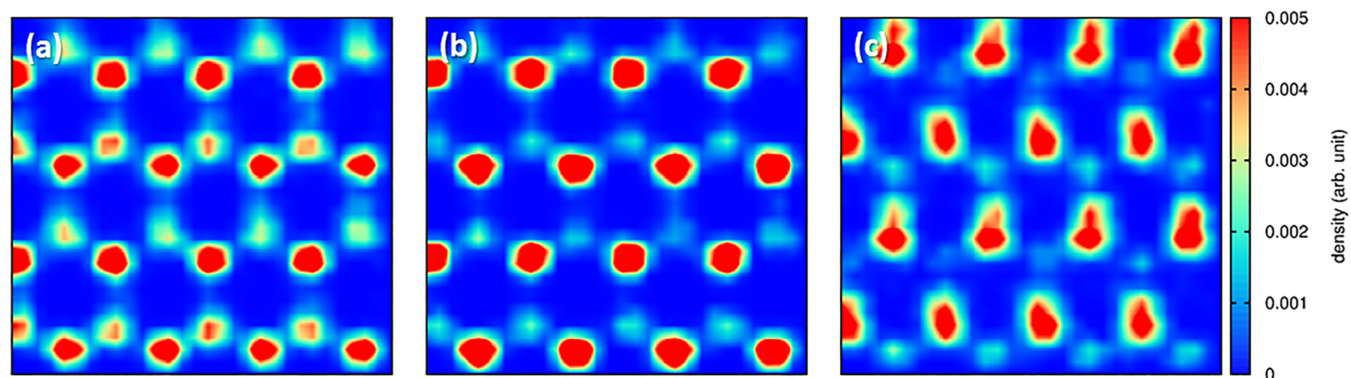


**Figure 12.** Fluorine density plots calculated with AIMD simulations in  $\text{SrF}_2$  in the superionic  $\epsilon$  phase at  $T = 2000$  K and  $P = 7.5$  GPa. Plots (a)–(c) were obtained by accumulating statistics over the three system partitions sketched in Figure 9b.

that, when combined together, form a regular two-dimensional hexagonal lattice. The preferred paths for interstitial diffusion, as given by the medium- and low-density regions in Figure 12, appear to be highly directional and oriented along the edges of the created hexagons (in the middle of which lay the  $\text{Sr}^{2+}$  ions). Ionic diffusion along the main  $a$  axis also seems possible due to the presence of repeated density patterns (although with gradual intensity) in all three system partitions.

The fluorine density plots obtained in  $\epsilon$ - $\text{CaF}_2$  display markedly different features from those just explained for  $\epsilon$ - $\text{SrF}_2$  (see Figure 11). For instance, the projected equilibrium positions now form very distorted hexagonal-like patterns that change appreciably from one supercell partition to the next. (In some cases, even it is not possible to identify regular polygons, see Figure 11b.) This result, which represents a signature of the  $\delta$  phase, may be thought of as a redistribution of  $\text{F}^-$  ions along the main  $a$  axis of the parent  $\gamma$  phase (see Figure 9b). Meanwhile, the diffusivity mechanisms involved in ionic transport appear to be quite similar to the ones just described for  $\epsilon$ - $\text{SrF}_2$  (although ionic diffusion along the main  $a$  axis of the parent  $\gamma$  phase now is significantly reduced, as suggested by the disappearance of alike density patterns in all three slices). The intermediate scattering function results enclosed in Figure 13b,c show that  $F_F$  decays also as an exponential function at long simulation times both in  $\epsilon$ - $\text{CaF}_2$  and  $\epsilon$ - $\text{SrF}_2$ . Thus, superionicity in highly compressed AEM difluorides appears to occur also as discrete and coordinated fluorine ion hops between neighboring interstitial sites, analogously to what is observed in the cubic  $\beta$  phase.

From the comparisons of Figures 11 and 12, it is clear that the superionic state in highly compressed  $\text{CaF}_2$  and  $\text{SrF}_2$

(also in  $\text{BaF}_2$ ) comes stabilized from a different phase. As we have already noted in section III.A, this is a direct consequence of the existence (absence) of the  $\delta$  phase in the phase diagram of  $\text{CaF}_2$  ( $\text{SrF}_2$  and  $\text{BaF}_2$ ). Our tentative explanation for such a phase-related effect across the AEM difluoride series is based on the loss of fluorine packing efficiency when moving from  $\text{Ca}^{2+}$  to other cationic species with larger ionic radius. We further discuss this point in the next section by presenting and analyzing the results of additional first-principles calculations.

#### IV. DISCUSSION

We have surveyed the series of  $P$ -induced solid–solid phase transitions occurring in AEM dihalides ( $\text{AB}_2$ ,  $A = \text{Mg, Ca, Sr, Ba}$  and  $B = \text{F, Cl, Br, I}$ ) at low temperatures, and we have found clear correlations between those and the materials descriptor  $\eta(A,B) \equiv r_A/r_B$ . Specifically, when  $\eta$  is larger than approximately 0.58, the corresponding compound (e.g.,  $\text{SrCl}_2$  and  $\text{BaBr}_2$ ) stabilizes either in the cubic  $\alpha$  or orthorhombic  $\gamma$  phase at zero pressure; compounds with high  $\eta$ 's ( $\geq 0.76$ ) adopt the  $\alpha$  phase (e.g.,  $\text{BaF}_2$ ), whereas compounds with  $\eta$ 's comprised between 0.76 and 0.58 can be found either in the  $\alpha$  or  $\gamma$  phases (e.g.,  $\text{SrCl}_2$  and  $\text{BaI}_2$  possess  $\eta$  values of around 0.6 but are found in the fluorite and contunnite structures, respectively). If  $\eta$  is smaller than approximately 0.58, then the corresponding system (e.g.,  $\text{CaI}_2$  and  $\text{MgCl}_2$ ) is energetically most stable in a phase with lower crystal symmetry than the cubic fluorite structure (e.g.,  $\text{CaI}_2$  adopts a rhombohedral  $P\bar{3}m1$  phase). Based on the experimental and theoretical evidence reported in the literature, AEM dihalides always appear to follow the phase-transition sequence  $\text{LS} \rightarrow \alpha \rightarrow \gamma$  as induced by pressure (postcontunnite

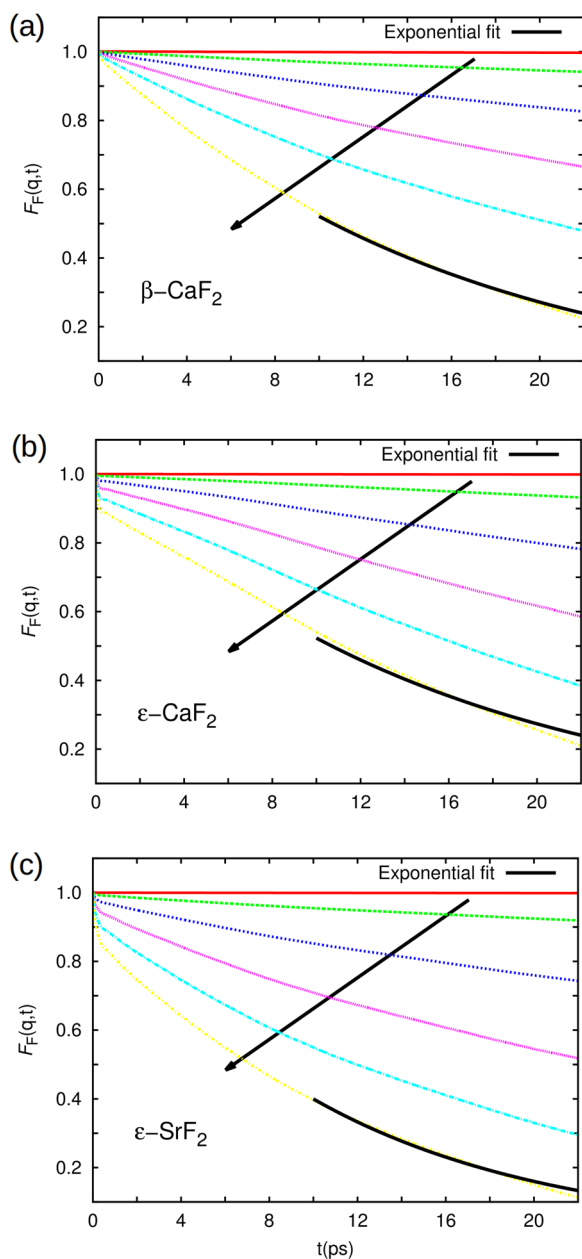


**Figure 13.** Intermediate scattering function calculated for fluorine ions in different superionic compounds and crystalline phases expressed as a function of wavevector,  $q$ , and time,  $t$ : (a)  $\beta$ - $\text{CaF}_2$ , (b)  $\epsilon$ - $\text{CaF}_2$ , and (c)  $\epsilon$ - $\text{SrF}_2$ . Wavevector values ranging from small to large (from top to bottom, as indicated by the black arrow) were considered in the calculations. The solid black lines correspond to exponential fits to the  $F_F(q, t)$  data obtained at long simulation times.

phases have been disregarded here), where “LS” stands for the low-symmetry phases observed in  $\eta \lesssim 0.58$  compounds, and the starting point for each compound corresponds to its zero-pressure phase. We note that the order in such a phase-transition sequence never is reversed by effect of compression.

We enclose the  $\eta$ -map of AEM dihalides,  $\text{AB}_2$ , in Figure 14; the corresponding effective ionic radii have been taken from ref 51. In particular, we represent the  $A$  species in the abscissa, the  $B$  species in the ordinate, and the resulting  $\eta(A,B)$  parameter as a three-dimensional surface (see colormap therein). We have applied a spline-based interpolation to the discrete set of  $\eta$  points because any arbitrary  $r_A/r_B$  value in principle can

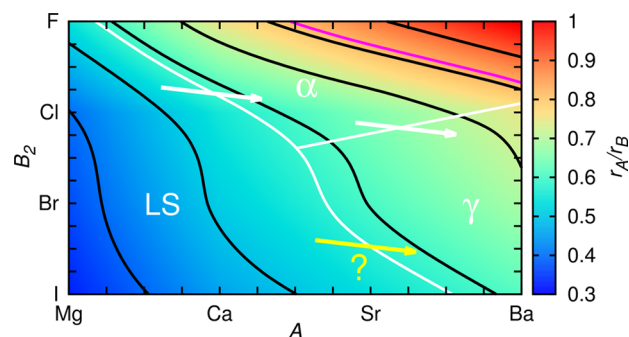


**Figure 14.** Generalized phase diagram of alkaline earth metal dihalides ( $\text{AB}_2$ ) under pressure expressed as a function of the ionic radius ratio  $\eta \equiv r_A/r_B$ . The black lines represent iso- $\eta$  curves. Letters in white stand for the phases observed at low- $T$  and low- $P$  conditions in the corresponding compounds (see text); “LS” is an acronym for low-symmetry phases (see text). The white lines indicate phase boundaries and the white arrows the structural trends observed under compression. The yellow arrow indicates a likely but experimentally not yet observed pressure-induced structural trend. The magenta line represents a tentative phase boundary for the compounds which may not exhibit the  $\delta$  phase at high- $T$ –high- $P$  conditions (namely, those fulfilling  $r_A/r_B \geq 0.82$ ). The ionic radius increases from left to right (for  $A$  elements) and from top to bottom (for  $B$  elements).

be obtained in practice by mixing different AEM dihalides. For instance, an effective  $\eta$  value of 0.85 can be realized in a 50%  $\text{CaF}_2$ – $\text{SrF}_2$  solid-solution prepared by ball milling,<sup>52</sup> namely,  $\text{Ca}_{0.5}\text{Sr}_{0.5}\text{F}_2$  (where the effective  $A$  ionic radius has been estimated straightforwardly by using Vegard’s law based on a linear interpolation,<sup>53</sup> namely,  $r_A = \frac{1}{2}r_{\text{Ca}} + \frac{1}{2}r_{\text{Sr}}$ ). The thick white lines in Figure 14 indicate the stability regions of AEM dihalides in the LS,  $\alpha$ , and  $\gamma$  phases at low- $T$  and low- $P$  conditions. The fact that the observations on the phase stability of AEM dihalides at equilibrium can be fairly mapped into a  $\eta$ -representation comes to support the validity of using  $r_A/r_B$ -based arguments in the present context. Meanwhile, the white arrows in Figure 14 indicate the observed phase-transition trends as induced by pressure, namely,  $\text{LS} \rightarrow \alpha \rightarrow \gamma$ . We note that the first part of such a phase-transition sequence ( $\text{LS} \rightarrow \alpha$ ) appears to correlate with an increase in  $\eta$ , whereas the second part ( $\alpha \rightarrow \gamma$ ) with a decrease in  $\eta$ . According to crystal-chemistry arguments, such  $P$ -induced phase transitions can be understood in terms of the usual facts that the cations normally are more compressible than the anions and that under compression the systems evolve toward more compact structures.<sup>54</sup> Therefore,  $P$ -induced phase transitions in AEM dihalides are expected to occur from the corresponding ambient-pressure phase to a structure located in a direction pointing toward the right and abscissa in the  $\eta$ -diagram (as is shown by the white arrows in Figure 14).

Based on our previous reflections, we wondered whether some of the LS compounds situated in the lower part of the diagram in Figure 14, mainly AEM diiodides, could transition directly into the  $\gamma$  phase by effect of pressure, as due to their proximity in  $\eta$ -space to the contunnite region (see question mark and yellow arrow in Figure 14). It is worth noticing that, to the best of our knowledge, no pressure-induced  $\text{LS} \rightarrow \gamma$  phase transition has been ever reported in AEM dihalides; also, it is true, however, that the high- $P$  behavior of compounds like AEM diiodides remain largely unexplored to date. In Figure 15, we show our relative enthalpy results obtained in  $\text{CaI}_2$  at zero temperature with DFT methods. As noted earlier, the ground-state of  $\text{CaI}_2$  corresponds to a rhombohedral  $P\bar{3}m1$

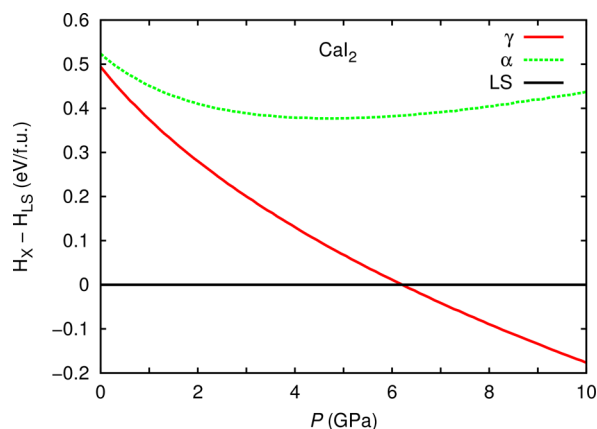


**Figure 15.** Zero-temperature enthalpy of  $\text{CaCl}_2$  under pressure considering different crystal structures. Pressure-induced  $\text{LS} \rightarrow \gamma$  phase transition is predicted to occur at  $P = 6.2$  GPa.

phase (space group 164) with  $Z = 1$ . We have considered the energetic stability of this compound in the  $\alpha$  and  $\gamma$  phases as referred to the rhombohedral ground state (other possible candidate structures have been disregarded). Our calculations actually predict a  $\text{LS} \rightarrow \gamma$  phase transition at  $P_i(0) = 6.2$  GPa. In spite of the fact that our analysis considers a quite small number of possible candidate structures, it clearly shows that the  $\gamma$  phase is energetically preferred over the  $\alpha$  phase in AEM dihalides under pressure. Therefore, it remains to be experimentally checked whether a  $P$ -induced  $\text{LS} \rightarrow \gamma$  phase transition actually occurs or not in  $\text{CaCl}_2$ . This latter zero-temperature outcome comes to show that the  $\eta$ -map shown in Figure 14 is not only useful for understanding the phase-transition trends across the AEM dihalides series but also for making coherent predictions.

Now we comment on the possible existence of the high- $P$ –high- $T$   $\delta$  phase in AEM dihalides. As we have discussed in previous sections, we have rationalized the existence (absence) of the  $\delta$  phase in highly compressed  $\text{CaF}_2$  ( $\text{SrF}_2$  and  $\text{BaF}_2$ ) in terms of a structural–distortion mechanism that facilitates the stabilization of the superionic state at elevated temperatures. In particular, the  $\delta$  phase allows for the creation of interstitial sites within the contunnite structure in small- $\eta$  compounds, where the amount of excess volume is reduced. Based on our first-principles results obtained for the phase diagram of AEM difluorides and by assuming the correctness of  $\eta$ -based arguments, we can make the hypothesis that the  $\delta$  phase will appear in compounds with  $r_A/r_B$  ratios smaller than  $\sim 0.82$ ; such a  $\eta$  threshold value corresponds to the interpolation between those of  $\text{CaF}_2$  and  $\text{SrF}_2$  (see magenta line in Figure 14). The consequence of this hypothesis being correct is that the number of AEM dihalides in which the  $\delta$  phase will appear would surpass the number of compounds in which it will not (that is, in Figure 14 the area involving  $\eta \gtrsim 0.82$  compounds is much smaller than the area involving  $\eta \lesssim 0.82$  compounds). In order to test this hypothesis, we performed additional AIMD simulations in  $\text{SrCl}_2$  under pressure (see Figure 16), for which  $\eta = 0.65$ . Specifically, we ran our simulations at a pressure of approximately 14 GPa, conditions at which the system stabilizes in the contunnite phase at zero temperature, and considered several temperature points taken at intervals of 250 K. As is shown in Figure 16,  $\gamma$ - $\text{SrCl}_2$  undergoes a structural transformation at a temperature close to 2500 K, which is very similar to the one originally found in  $\gamma$ - $\text{CaF}_2$  and which we identified with a  $T$ -induced solid–solid ( $\gamma \rightarrow \delta$ ) phase transition (see Figure 4

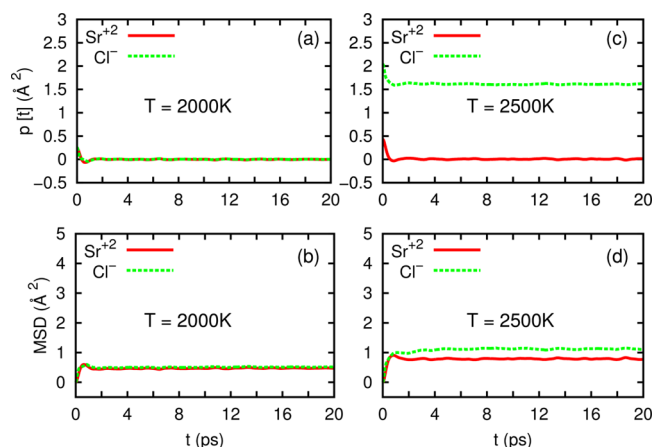


**Figure 16.** Position correlation function and mean squared displacement calculated in  $\text{SrCl}_2$  with AIMD simulations at  $T = 2000$  K (a,b) and 2500 K (c,d) [ $P = 14(1)$  GPa]. At 2000 (2500) K, the system is in the  $\gamma$  ( $\delta$ ) phase (see text).

in ref 11). In particular, the sublattice of  $\text{Cl}^-$  ions becomes vibrationally unstable, as is illustrated by the corresponding ionic position correlation functions in Figure 16c, but ionic diffusion is not observed in the crystal, as can be appreciated in the MSD plots in Figure 16d. We can actually identify those structural and ion-transport features with the occurrence a  $\gamma \rightarrow \delta$  phase transition in  $\text{SrCl}_2$ . Since the value of the  $\eta$  parameter in  $\text{SrCl}_2$  amounts to 0.65, which actually is smaller than the critical threshold value of  $\sim 0.82$  defined above, our arguments and predictions in the present discussion appear to be fully consistent and meaningful.

## V. CONCLUSIONS

We have presented a comprehensive first-principles computational study on the high- $P$ –high- $T$  phase diagram of AEM difluorides, namely,  $\text{CaF}_2$ ,  $\text{SrF}_2$ , and  $\text{BaF}_2$ . Our results show that at moderate pressures the superionic behavior of  $\text{SrF}_2$  and  $\text{BaF}_2$  in the  $\beta$  phase differ appreciably from that previously reported for  $\text{CaF}_2$ , since no  $P$ -induced depletion of the superionic critical temperature is found in them. The high- $P$ –high- $T$   $\delta$  phase, previously observed in  $\text{CaF}_2$ , neither appears in the phase diagram of  $\text{SrF}_2$  nor  $\text{BaF}_2$ . We have rationalized the origins of this phase-related effect across the AEM difluorides series in terms of the  $r_A/r_B$  parameter and packing-efficiency based arguments. Intensive *ab initio* molecular dynamics simulations, which fully take into account anharmonicity, have been conducted in order to describe at the atomic scale the ionic diffusivity mechanisms occurring in the superionic phases of AEM difluorides, namely,  $\beta$  and  $\epsilon$ , at moderate and high pressures, respectively. Moreover, we have shown that simple physical arguments based on intuitive ionic-radii comparisons are in fact very useful to explain and foresee phase transition trends in AEM dihalides ( $\text{AB}_2$ ,  $A = \text{Mg, Ca, Sr, Ba}$  and  $B = \text{F, Cl, Br, I}$ ), and related solid solutions ( $\text{A}_x\text{A}'_{1-x}\text{B}_y\text{B}'_{2-y}$ ), under pressure. In particular, we have predicted the possibility of a  $P$ -induced  $\text{LS} \rightarrow \alpha$  phase transition in AEM dihalides, which has not been observed previously, and the stabilization of the  $\delta$  phase at high- $P$ –high- $T$  conditions in a large number of AEM dihalides (that is, those fulfilling the condition  $\eta \lesssim 0.82$ ). We hope that our computational first-principles study will motivate future characterization experiments in AEM dihalides at high- $P$  and high- $T$  conditions.

## ■ APPENDIX: AEM DIFLUORIDE CLASSICAL POTENTIALS

The interatomic potentials that we adopted to simulate SrF<sub>2</sub> and BaF<sub>2</sub> with molecular dynamics were of the Born–Mayer–Huggins (BMH) form, namely:

$$V_{ij}(r) = A_{ij} e^{-r/\rho_{ij}} - \frac{C_{ij}}{r^6} + \frac{Z_i Z_j}{r} \quad (\text{A1})$$

where subscripts *i* and *j* represent the ionic species in the system and *r* is the radial distance between a couple of atoms. Each pairwise interatomic potential is composed of three different terms; the first one is of exponential type and accounts for the short-ranged atomic repulsion deriving from the overlapping between electron clouds; the second term is proportional to *r*<sup>−6</sup> and represents the long-ranged atomic attraction due to dispersive van der Waals forces; the third term is the usual Coulomb interaction between point atomic charges. The value of the corresponding BMH potential parameters *A*, *C*, and *Z* are reported in Table A1.

**Table A1. Born–Mayer–Huggins Interatomic Potential Parameters Used To Describe SrF<sub>2</sub> and BaF<sub>2</sub> in Our Classical Molecular Dynamics Simulations<sup>a</sup>**

	<i>A</i> (eV)	<i>ρ</i> (Å)	<i>C</i> (eV·Å <sup>6</sup> )
SrF <sub>2</sub>			
Sr <sup>+</sup> –F <sup>−</sup>	1751.790	0.30378	0.10006
F <sup>−</sup> –F <sup>−</sup>	2094.048	0.25663	16.34243
Sr <sup>+</sup> –Sr <sup>+</sup>	0.0	0.0	0.0
BaF <sub>2</sub>			
Ba <sup>+</sup> –F <sup>−</sup>	2655.510	0.29516	0.09287
F <sup>−</sup> –F <sup>−</sup>	1161.257	0.34074	31.78328
Ba <sup>+</sup> –Ba <sup>+</sup>	0.0	0.0	0.0

<sup>a</sup>Ionic charges are *Z*<sub>Sr</sub> = *Z*<sub>Ba</sub> = +2, and *Z*<sub>F</sub> = −1, as expressed in units of *e*.

The BMH potential parameters reported in Table A1 were determined through a matching algorithm<sup>55–58</sup> based on a least-square fit, to reproduce as close as possible a set of DFT reference data containing total energies and atomic forces. The objective function in our optimization procedure, which needs to be minimized, is expressed as

$$\chi^2 = \omega_E \sum_i^N \frac{(E_i^{\text{FF}} - E_i^{\text{DFT}})^2}{\sum_j^N (E_j^{\text{DFT}} - \langle E^{\text{DFT}} \rangle)^2} + \omega_F \sum_i^N \frac{\sum_{l,\alpha}^{n,3} (F_{l\alpha,i}^{\text{FF}} - F_{l\alpha,i}^{\text{DFT}})^2}{\sum_{l,\alpha,j}^{n,3,N} (F_{l\alpha,j}^{\text{DFT}} - \langle F^{\text{DFT}} \rangle)^2} \quad (\text{A2})$$

where *N* = 20 is the number of reference configurations, *n* = 192 is the number of particles in each configuration, and *ω*<sub>E</sub> and *ω*<sub>F</sub> are weights assigned to the energy, *E*, and force, *F*, contributions to  $\chi^2$ , respectively. Subscripts “DFT” and “FF” refer to the results obtained with DFT and the corresponding BMH potential, respectively. With such a definition of the objective function, we ensured that despite different magnitudes are expressed in different units, all them were normalized and contributed equitably to  $\chi^2$ . After some tests, we decided to constrain the values of *ω*<sub>E</sub> and *ω*<sub>F</sub> to 1.0 and 0.5, respectively. The set of *N* reference configurations comprised several structures employed for the calculation of the vibrational phonon spectra of each compound, both in the fluorite and contunnite

phases, as obtained with the “direct approach” (see section II.A). The BMH potential parameters were varied during the minimization of the objective function  $\chi^2$  according to a quadratic polynomial interpolation line-search based on the Broyden–Fletcher–Goldfarb–Shanno formula.<sup>59</sup> The minimizations were finalized once all the gradients of the objective function were smaller than 10<sup>−5</sup> in absolute value. Typically, this was achieved within ~1000 minimization loops when starting from a reasonable initial guess for the BMH potential parameters.

The performance of such BMH potentials in reproducing the superionic and melting properties of SrF<sub>2</sub> and BaF<sub>2</sub> under pressure, as estimated with first-principles methods, is reasonably good (although not perfect). For instance, in SrF<sub>2</sub> the transition temperatures *T*<sub>s</sub> and *T*<sub>m</sub> obtained with molecular dynamics systematically are about 200–400 K larger than the values obtained with first-principles methods. In BaF<sub>2</sub>, the agreement between those transition temperatures as obtained with molecular dynamics and first-principles methods is very good in the cubic fluorite phase (i.e., discrepancies amounting to within 100 K), but not so in the orthorhombic contunnite phase (i.e., discrepancies amounting to within 300–600 K).

## ■ AUTHOR INFORMATION

### ORCID

Claudio Cazorla: 0000-0002-6501-4513

Daniel Errandonea: 0000-0003-0189-4221

### Notes

The authors declare no competing financial interest.

## ■ ACKNOWLEDGMENTS

This research was supported under the Australian Research Council’s Future Fellowship funding scheme (No. FT140100135), the National Science Foundation (No. IIA-1357113), the Spanish government MINECO, the Spanish Agencia Estatal de Investigación (AEI), and the Fondo Europeo de Desarrollo Regional (FEDER) (No. MAT2016-75586-C4-1-P and MAT2015-71070-REDC). C.C. and D.E. also acknowledge support from the University of Valencia through the grant UV-INV-EPC17-547792. Computational resources and technical assistance were provided by the Australian Government and the Government of Western Australia through Magnus under the National Computational Merit Allocation Scheme and The Pawsey Supercomputing Centre.

## ■ REFERENCES

- (1) Hull, S. Superionics: crystal structures and conduction processes. *Rep. Prog. Phys.* **2004**, *67*, 1233.
- (2) Wachsmann, E. D.; Lee, K. T. Lowering the temperature of oxide solid fuel cells. *Science* **2011**, *334*, 935.
- (3) Kamaya, N.; Homma, K.; Yamakawa, Y.; Hirayama, M.; Kanno, R.; Yonemura, M.; Kamiyama, T.; Kato, Y.; Hama, S.; Kawamoto, K.; Mitsui, A. A lithium superionic conductor. *Nat. Mater.* **2011**, *10*, 682.
- (4) Wang, Y.; Richards, W. D.; Ong, S. P.; Miara, L. J.; Kim, J. C.; Mo, Y.; Ceder, G. Design principles for solid-state lithium superionic conductors. *Nat. Mater.* **2015**, *14*, 1026.
- (5) Urban, A.; Seo, D.-H.; Ceder, G. Computational understanding of Li-ion batteries. *NPJ. Comp. Mater.* **2016**, *2*, 16002.
- (6) Sagotra, A. K.; Cazorla, C. Stress-mediated enhancement of ionic conductivity in fast-ion conductors. *ACS Appl. Mater. Interfaces* **2017**, *9*, 38773.
- (7) Cazorla, C. In the search of new electrocaloric materials: Fast ion conductors. *Results Phys.* **2015**, *5*, 262.
- (8) Cazorla, C.; Errandonea, D. Giant mechanocaloric effects in fluorite-structured superionic materials. *Nano Lett.* **2016**, *16*, 3124.

- (9) Sagotra, A. K.; Errandonea, D.; Cazorla, C. Mechanocaloric effects in superionic thin films from atomistic simulations. *Nat. Commun.* **2017**, *8*, 963.
- (10) Aznar, A.; Lloveras, P.; Romanini, M.; Barrio, M.; Tamarit, J. Ll.; Cazorla, C.; Errandonea, D.; Mathur, N. D.; Planes, A.; Moya, X.; Manosa, Ll. Giant barocaloric effects over a wide temperature range in superionic conductor AgI. *Nat. Commun.* **2017**, *8*, 1851.
- (11) Cazorla, C.; Errandonea, D. Superionicity and polymorphism in calcium fluoride at high pressure. *Phys. Rev. Lett.* **2014**, *113*, 235902.
- (12) Derrington, C. E.; Lindner, A.; O'Keefe, M. Ionic conductivity of some alkaline earth halides. *J. Solid State Chem.* **1975**, *15*, 171.
- (13) Hayes, W.; Hutchings, M. T. *Ionic Solids at High Temperatures*; World Scientific: Singapore, 1985.
- (14) Evangelakis, G. A.; Pontikis, V. Direct computation of the superionic conductivity in CaF<sub>2</sub> by constant-temperature equilibrium and nonequilibrium molecular dynamics. *Europhys. Lett.* **1989**, *8*, 599.
- (15) McLaughlan, S. D. Electron paramagnetic resonance of trivalent-rare-earth-monovalent-alkaline-earth ion pairs in CaF<sub>2</sub>. *Phys. Rev.* **1967**, *160*, 287.
- (16) Mitchell, A.; Joshi, S. The densities of melts in the systems CaF<sub>2</sub>-CaO and CaF<sub>2</sub>-Al<sub>2</sub>O<sub>3</sub>. *Metall. Trans. A* **1972**, *3*, 2306.
- (17) Nelson, J. R.; Needs, R. J.; Pickard, C. J. High-pressure phases of group-II difluorides: Polymorphism and superionicity. *Phys. Rev. B: Condens. Matter Mater. Phys.* **2017**, *95*, 054118.
- (18) Perdew, J. P.; Burke, K.; Ernzerhof, M. Generalized gradient approximation made simple. *Phys. Rev. Lett.* **1996**, *77*, 3865.
- (19) Kresse, G.; Furthmüller, J. Efficient iterative schemes for ab initio total-energy calculations using a plane-wave basis set. *Phys. Rev. B: Condens. Matter Mater. Phys.* **1996**, *54*, 11169.
- (20) Blöchl, P. E. Projector augmented-wave method. *Phys. Rev. B: Condens. Matter Mater. Phys.* **1994**, *50*, 17953.
- (21) Kresse, G.; Fürthmüller, J.; Hafner, J. Ab initio force constant approach to phonon dispersion relations of diamond and graphite. *Europhys. Lett.* **1995**, *32*, 729.
- (22) Alfè, D.; Price, G. D.; Gillan, M. J. Thermodynamics of hexagonal-close-packed iron under Earth's core conditions. *Phys. Rev. B: Condens. Matter Mater. Phys.* **2001**, *64*, 045123.
- (23) Alfè, D. PHON: A program to calculate phonons using the small displacement method. *Comput. Phys. Commun.* **2009**, *180*, 2622.
- (24) Cazorla, C.; Boronat, J. Simulation and understanding of atomic and molecular quantum crystals. *Rev. Mod. Phys.* **2017**, *89*, 035003.
- (25) Cazorla, C.; Errandonea, D. The high-pressure high-temperature phase diagram of CaF<sub>2</sub> from classical atomistic simulations. *J. Phys. Chem. C* **2013**, *117*, 11292.
- (26) Belonoshko, A. B.; Skorodumova, N. V.; Rosengren, A.; Johansson, B. Melting and critical superheating. *Phys. Rev. B: Condens. Matter Mater. Phys.* **2006**, *73*, 012201.
- (27) Cazorla, C.; Alfè, D.; Gillan, M. J. Constraints on the phase diagram of molybdenum from first-principles free-energy calculations. *Phys. Rev. B: Condens. Matter Mater. Phys.* **2012**, *85*, 064113.
- (28) Cazorla, C.; Gillan, M. J.; Taioli, S.; Alfè, D. Ab initio melting curve of molybdenum by the phase coexistence method. *J. Chem. Phys.* **2007**, *126*, 194502.
- (29) Taioli, S.; Cazorla, C.; Gillan, M. J.; Alfè, D. Melting curve of tantalum from first principles calculations. *Phys. Rev. B: Condens. Matter Mater. Phys.* **2007**, *75*, 214103.
- (30) Cazorla, C.; Alfè, D.; Gillan, M. J. Melting properties of a simple tight-binding model of transition metals: I. The region of half-filled d-band. *J. Chem. Phys.* **2009**, *130*, 174707.
- (31) Alfè, D.; Cazorla, C.; Gillan, M. J. The kinetics of homogeneous melting beyond the limit of superheating. *J. Chem. Phys.* **2011**, *135*, 024102.
- (32) Alfè, D. Temperature of the inner-core boundary of the Earth: Melting of iron at high pressure from first-principles coexistence simulations. *Phys. Rev. B: Condens. Matter Mater. Phys.* **2009**, *79*, 060101.
- (33) Morris, J. R.; Wang, C. Z.; Ho, K. M.; Chan, C. T. Melting line of aluminum from simulations of coexisting phases. *Phys. Rev. B: Condens. Matter Mater. Phys.* **1994**, *49*, 3109.
- (34) Belonoshko, A. B. Molecular dynamics of MgSiO<sub>3</sub> perovskite at high pressures: Equation of state, structure, and melting transition. *Geochim. Cosmochim. Acta* **1994**, *58*, 4039.
- (35) Belonoshko, A. B. Molecular dynamics of silica at high pressures: Equation of state, structure, and phase transitions. *Geochim. Cosmochim. Acta* **1994**, *58*, 1557.
- (36) Cazorla, C.; Alfè, D.; Gillan, M. J. Comment on Molybdenum at high pressure and temperature: Melting from another solid phase. *Phys. Rev. Lett.* **2008**, *101*, 049601.
- (37) Mikhaylushkin, A. S.; Simak, S. I.; Burakovskiy, L.; Chen, S. P.; Johansson, B.; Preston, D. L.; Swift, D. C.; Belonoshko, A. B. Molybdenum at high pressure and temperature: melting from another solid phase. *Phys. Rev. Lett.* **2008**, *101*, 049602.
- (38) Errea, I.; Rousseau, B.; Bergara, A. Anharmonic stabilization of the high-pressure simple cubic phase of calcium. *Phys. Rev. Lett.* **2011**, *106*, 165501.
- (39) Errea, I. Approaching the strongly anharmonic limit with ab initio calculations of materials' vibrational properties - a colloquium. *Eur. Phys. J. B* **2016**, *89*, 237.
- (40) Voronin, B. M.; Volkov, S. V. Ionic conductivity of fluorite type crystals CaF<sub>2</sub>, SrF<sub>2</sub>, BaF<sub>2</sub>, and SrCl<sub>2</sub> at high temperatures. *J. Phys. Chem. Solids* **2001**, *62*, 1349.
- (41) Huang, X.-Y.; Cheng, X.-L.; Fan, C.-L.; Chen, Q.; Yuan, X.-L. Molecular Dynamics Simulations for Melting Temperatures of SrF<sub>2</sub> and BaF<sub>2</sub>. *Chin. J. Chem. Phys.* **2009**, *22*, 310.
- (42) Evangelakis, G. A. and Demitrios Miliotis. Ionic and superionic conductivities of SrF<sub>2</sub> crystals in a wide frequency range. *Phys. Rev. B: Condens. Matter Mater. Phys.* **1987**, *36*, 4958.
- (43) Castiglione, M. J.; Wilson, M.; Madden, P. A.; Grey, C. P. Ion mobility in  $\alpha$ -PbF<sub>2</sub>: a computer simulation study. *J. Phys.: Condens. Matter* **2001**, *13*, 51.
- (44) Castiglione, M. J.; Madden, P. A. Fluoride ion disorder and clustering in superionic PbF<sub>2</sub>. *J. Phys.: Condens. Matter* **2001**, *13*, 9963.
- (45) Düvel, A. V.; Heitjans, P.; Fedorov, P.; Scholz, G.; Cibir, G.; Chadwick, A. V.; Pickup, D. M.; Ramos, S.; Sayle, L. W. L.; Sayle, E. K. L.; Sayle, T. X. T.; Sayle, D. C. Is geometric frustration-induced disorder a recipe for high ionic conductivity? *J. Am. Chem. Soc.* **2017**, *139*, 5842.
- (46) Gillan, M. J. The Simulation of Superionic Materials. *Physica B + C* **1985**, *131*, 157.
- (47) Wolf, M. L.; Walker, J. R.; Catlow, C. R. A. A Molecular Dynamics Simulation Study of the Superionic Conductor Lithium Nitride: I. *J. Phys. C: Solid State Phys.* **1984**, *17*, 6623.
- (48) Rowe, J. M.; Sköld, K.; Flotow, H. E.; Rush, J. J. Quasielastic neutron scattering by hydrogen in the  $\alpha$  and  $\beta$  phases of vanadium hydride. *J. Phys. Chem. Solids* **1971**, *32*, 41.
- (49) Hutchings, M. T.; Clausen, K.; Dickens, M. H.; Hayes, W.; Kjems, J. K.; Schnabel, P. G.; Smith, C. Investigation of thermally induced anion disorder in fluorites using neutron scattering techniques. *J. Phys. C: Solid State Phys.* **1984**, *17*, 3903.
- (50) Goff, J. P.; Hayes, W.; Hull, S.; Hutchings, M. T. Neutron powder diffusion study of the fast-ion transition and specific heat anomaly in beta-lead fluoride. *J. Phys.: Condens. Matter* **1991**, *3*, 3677.
- (51) Shannon, R. D. Revised effective ionic radii and systematic studies of interatomic distances in halides and chalcogenides. *Acta Crystallogr., Sect. A: Cryst. Phys., Diffr., Theor. Gen. Crystallogr.* **1976**, *A32*, 751.
- (52) Ruprecht, B.; Wilkening, M.; Steuernagel, S.; Heitjans, P. Anion diffusivity in highly conductive nanocrystalline BaF<sub>2</sub>:CaF<sub>2</sub> composites prepared by high-energy ball milling. *J. Mater. Chem.* **2008**, *18*, 5412.
- (53) Vegard, L. Die Konstitution der Mischkristalle und die Raumfüllung der Atome. *Eur. Phys. J. A* **1921**, *5*, 17.
- (54) Errandonea, D.; Manjón, F. J. Pressure effects on the structural and electronic properties of ABX<sub>4</sub> scintillating crystals. *Prog. Mater. Sci.* **2008**, *53*, 711.
- (55) Ercolessi, F.; Adams, J. B. Interatomic Potentials from First-Principles Calculations: The Force-Matching Method. *Europhys. Lett.* **1994**, *26*, 583.

(56) Sala, J.; Guàrdia, E.; Martí, J.; Spångberg, D.; Masia, M. Fitting properties from density functional theory based molecular dynamics simulations to parameterize a rigid water force field. *J. Chem. Phys.* **2012**, *136*, 054103.

(57) Masia, M.; Guàrdia, E.; Nicolini, P. The force matching approach to multiscale simulations: Merits, shortcomings, and future perspectives. *Int. J. Quantum Chem.* **2014**, *114*, 1036.

(58) Cazorla, C.; Boronat, J. First-principles modeling of three-body interactions in highly compressed solid helium. *Phys. Rev. B: Condens. Matter Mater. Phys.* **2015**, *92*, 224113.

(59) Nocedal, J.; Wright, S. J. *Numerical Optimization*; Springer: Berlin, 2006.